Article

Porous Metal-Organic Frameworks for Enhanced Performance Silicon Anodes in Lithium-ion Batteries

Romeo Malik, Melanie J. Loveridge, Luke J. Williams, Qianye Huang, Geoff West, Paul R Shearing, Rohit Bhagat, and Richard I. Walton

Chem. Mater., **Just Accepted Manuscript** • DOI: 10.1021/acs.chemmater.9b00933 • Publication Date (Web): 15 May 2019

Porous Metal-Organic Frameworks for Enhanced Performance Silicon Anodes in Lithium-ion Batteries

Romeo Malik[a], Melanie. J. Loveridge[a], Luke J. Williams[b], Qianye Huang[a], Geoff West[a], Paul R. Shearing[c], Rohit Bhagat[a], Richard I. Walton[b]*

[a] WMG, University of Warwick, Gibbet Hill Road, Coventry CV4 7AL, UK

[b] Department of Chemistry, University of Warwick, Gibbet Hill Road, Coventry CV4 7AL, UK

[c] Department of Chemical Engineering, University College London, Torrington Place, London WC1E 7JE, UK

ABSTRACT

Maintaining the physical integrity of electrode microstructures in Li-ion batteries is critical to significantly extend their cycle life. This is especially important for high capacity anode materials such as silicon, whose operational volume expansion exerts huge internal stress within the anode, resulting in electrode destruction and capacity fade. In this study, we demonstrate that by incorporating metal-organic frameworks (MOFs) with carboxylate organic linkers into Si-based anodes, a stable and flexible pore network is generated to maximize and maintain Li-ion flux throughout the electrode's architecture. We show that the zirconium carboxylate MOF UiO-67 is a versatile co-material to boost performance and mitigate the rate of anode degradation that presently limits the lifetime of Si anodes. The cage-like pores in UiO-67 and flexural properties of the 4, 4'-biphenyldicarboxylate organic linker are proposed to create robust "ionophores" in the anode film to enhance longer-term durability and performance.

INTRODUCTION

The development of electrode components beyond the active materials (Li host particles) remains a comparatively less explored domain in Li-ion batteries. A considerable research effort has attempted to use silicon as an anode material, with a specific capacity of 3579 $mAhg^{-1}$ (compared with 372 $mAhg^{-1}$ for graphite).[1] However, there are significant detrimental issues associated with a massive volume expansion upon alloying silicon with Li^+ (up to 280%) resulting in pulverization and electrode degradation and failure.[2] Additionally, its surface continually reacts with the electrolyte ($\leq$ 0.9 V vs Li/Li^+) to form a solid-electrolyte interphase (SEI), which is a major source of Li loss and contributes to the performance degradation.

Attempts to circumnavigate the problems associated with silicon have broadly used two distinct approaches. The first involves the modification of the silicon morphology, including amorphous thin films,[3],[4] nanowires, macro-porosity, nano-sized silicon particles[5] and surface coatings.[6] The second approach focuses on the development of hybrid silicon anodes and includes composite development with variation in the silicon content, morphology, composite composition, preparation techniques, and dispersion methods. Additives include lithium-inactive materials,[7] lithium-active materials,[7] and various binder systems[7–9] as well as combining silicon with carbon materials.[10] However, the highly complex synthesis methods along with excessive manufacturing cost of these materials still poses practical questions for real applications.

In this paper, we report an investigation into how the electronic and ionic conductivity of silicon anodes may be optimized by incorporating metal-organic frameworks (MOFs) alongside carbon hierarchies. We reveal the beneficial effect of adding the structurally flexible MOF component to the composite, demonstrating improved mechanical properties via modification of the porosity. MOFs are a class of crystalline porous materials and have a unique combination of physical properties, namely high specific surface area, organic functional linkers and metal sites,[11] and with evidence pointing towards their application as electrode materials for electrochemical devices.[12–14] The tuneable pore structures and functional redox-active components of MOFs may conceivably make it possible for Li^+ ions to travel more homogenously through the anode.[15]

The practical use of redox-active MOFs in lithium-ion batteries (LIBs) as the primary Li host material is unrealistic for several reasons, namely, the low density, limited Li^+ ion insertion capability, poor electronic conductivity, and irreversible structural modification over multiple cycles.[14] Our rationale is to explore and understand MOFs for LIBs, as flexibility and porosity enhancing additives. The robust zirconium carboxylate MOFs, UiO-66 and UiO-67 were selected with the dual purpose of improving and maintaining the porous networks of the anode whilst enhancing the cohesion of the components. Both MOFs contain carboxylate organic linkers, chosen for the possible esterification reaction between the surface carboxylate groups in both the MOFs and in the polyacrylic acid (PAA binder) with silanol groups on the surface of Si in our electrode system.[16] Certain MOF materials, particularly UiO-66, have emerged as being stable with respect to conditions of temperature, water or other chemical environments. UiO-66 has also been shown to intercalate Li by way of interaction with the aromatic components of the constituent ligands.[11]

Pore distribution plays a key role in cell performance through the electrochemical reaction kinetics, as well as the electrode's transport properties.[17] Impedance spectroscopy and physical characterization are used to capture and quantify the evolution of internal morphology and the build-up of resistance.

EXPERIMENTAL SECTION

Synthesis of UiO-66: 1,4-Benzenedicarboxylic acid, 1.19 g, and zirconium(IV) chloride, 0.823 g, (2:1 molar ratio) were weighed and dissolved in *N*,*N*-dimethylformamide (50 ml). To this solution, 10 ml of hydrochloric acid (35%) was added and the resulting mixture was stirred at room temperature for 30 minutes. The reaction vessel was sealed inside a 200 ml Teflon-lined stainless-steel autoclave and heated under hydrothermal conditions, at 120 °C for 12 hours. The product was obtained as a white solid by filtration and subsequent washing with methanol and then dried in air at 70 °C. All chemicals were used as supplied by Sigma-Aldrich.

Synthesis of UiO-67: 4,4'-Biphenyldicarboxylic acid, 1.082 g, and zirconium(IV) chloride, 0.805 g, in a 1.3: 1 molar ratio, were dissolved in *N*,*N*-dimethylformamide (60 ml). To this solution, 6 ml

hydrochloric acid (35%) was added and the resulting mixture was stirred for 30 minutes at room temperature. Then, the reaction was heated at 80 °C under hydrothermal conditions in a 200 ml Teflon-lined stainless-steel autoclave for 24 hours. The product was obtained through filtration as a colorless solid, which was then stirred in *N*,*N*-dimethylformamide at 50 °C for 12 hours to remove unreacted biphenyl-4,4'-dicarboxylic acid, then filtered and washed with methanol, before drying at 70 °C overnight. All chemicals were used as supplied by Sigma-Aldrich.

Electrode Materials: The electrode slurry was prepared from silicon powder with average particle size of 2.2 μm (Elkem Silgrain e-Si), carbon black (Super C65, TIMCAL C-NERGY), graphite (SFG-6, TIMCAL C-NERGY), carbon nanotubes (Tuball Inc.) and few-layer graphene (FLG) (thickness of 6 - 8 nm, XG Sciences). A carbon mixture was made from 88% carbon nanotubes, 6% carbon black and 6% FLG in deionized water with a solids content of 64%. The heterogeneous carbon mixture was added to enhance both the long-range (planar) and the short-range (depth) conductivity of coating with a possible mechanical strengthening from graphene.[18] The aqueous binder was made from polyacrylic acid (PAA) powder (average Mw ~450,000, Sigma-Aldrich) and was partially neutralized to 70% with sodium hydroxide as proposed by Huang *et al.*[18]. The neutralization step is to extend the chain configuration of the PAA as it might affect the electrolytic dissolution and also the agglomeration of carboxyl groups in PAA from hydrogen bonding. The polymer chains in Na-PAA are stretched due to electrostatic repulsion and it also exhibits higher viscosity[19] improving adhesion in the electrode material.

Electrode Material Preparation: The additives were dispersed in a mixture of deionized water and isopropanol (1:5 wt%) and sonicated for 30 min to break any agglomerates. The electrode was prepared from a slurry of silicon powder, carbon mixture, additives suspension and water as the polymer binder solvent (for every 10 g of silicon 20 g of deionized water was added). The components were mixed in a high-speed Homodisperer (Model 2.5, PRIMIX) for 30 min at 1000 rpm. The resulting mixture was ultrasonically processed (UP400S, SciMED) for two periods at 60% amplitude for 7.5 min each. Following this, the Na-PAA binder solution was added to the solution prior to high-speed

homodispersion for 30 min at 1000 rpm. Finally, the slurry was transferred to a Filmix disperser (Model 40-40, PRIMIX, Japan) for homogenization and breakdown of any secondary agglomeration. This was a two-step process, first at 10 ms^{-1} for 30 secs and then at 25 ms^{-1} for 30 secs.

The coating process involved spreading the prepared slurry onto a current collector of copper foil (10 μm, Oak Mitsui, electrodeposited) using a draw-down coater with a spreading blade (K control coater Model 101, RK Print, UK). The blade gap between the blade tip and the copper foil can be adjusted between the ranges of 0 – 100 mm, for this study, a blade gap of 100 μm was used. After coating the slurry onto the copper foil, it was dried on a preheated hot plate, set at a temperature of 50 °C to eliminate any solvent. The coating was moved to a vacuum oven set at 50 °C for overnight drying to ensure maximum moisture removal.

Materials Characterization: Powder X-ray diffraction patterns were measured for sample identification using a Panalytical X'Pert Pro MPD, equipped with monochromatic Cu $K_{\alpha 1}$ radiation (λ = 1.54056 Å) and a PIXcel solid state detector. Combined thermogravimetric analysis (TGA) – differential scanning calorimetry (DSC) was performed using a Mettler Toledo TGA/DSC1 instrument under either ambient air pressure or nitrogen atmosphere, with a heating rate of 10 °C·min^{-1} from 25 °C to 1000 °C.

Electrochemical Testing: Electrodes were cut from vacuum dried electrodes in a dry room (with a dew point of -45° C) to ensure there was no exposure to moisture during the cell assembly process. The separator is PP/PE/PP microporous trilayer membrane (Celgard 2325) and the electrolyte used was RD265 (1.2 M $LiPF_6$ in ethyl carbonate/ethyl methyl carbonate (1/3 v/v), 15% fluoroethylene carbonate and 3% vinylene carbonate) (PuriEL, SoulBrain). The silicon half-cells were cycled against lithium (diameter = 15.6 mm, PI-KEM). For statistically reproducible results three half cells corresponding to each formulation were made. The mass of Si in the cut out dry electrode discs was 2.27±0.21 mg. The electrochemical cycling was characterized using a multi-channel potentiostat, VMP3 (Bio-Logic) at room temperature. The cells were charged and discharged using a constant current mode. For the first cycle a C-rate of C/20 was used to initiate SEI formation and from the second cycle, a rate of C/5 was

applied where C denotes capacity of the cell. A cut-off voltage of 50 mV was applied to avoid re-crystallizing $Li_{15}Si_4$ from highly lithiated amorphous silicon.[20] Electrodes from all the four formulations were cycled at 3 different silicon capacity, namely, 1200 $mAhg^{-1}$ (corresponding to a current density of 238 mA g^{-1} at C/5), 1800 $mAhg^{-1}$ (corresponding to a current density of 358 mA g^{-1} at C/5) and to the maximum experimental capacity of 3579 $mAhg^{-1}$ (corresponding to a current density of 716 mA g^{-1} at C/5). Cells were cycled at the full capacity of silicon to compare the effects of these additives towards capacity retention and cycle life under more extreme operational parameters, and also at 1800 $mAhg^{-1}$ and 1200 $mAhg^{-1}$ capacity limits to minimize any pulverization from large volume expansion upon lithiation[20] for improved cycle life. The upper cut-off voltage applied was 1 V to avoid any overcharging. Impedance measurements were carried out after the first cycle and for every 10 cycles. Potentiostatic electrochemical impedance spectroscopy (PEIS) measurement technique was applied together with galvanostatic cycling at 50% state of charge (during lithiation step by limiting lithiation to 2.5 hrs). The frequency range applied for this analysis was from 100 KHz up to 10 mHz (with 10 frequencies scanned per decade) with a sinus amplitude of 10 mV. The semicircle due to the SEI (R_{SEI}) can be identified between the frequency range of 100 kHz to 10 kHz, while the semicircle of the CT (R_{CT}) can be identified between the frequency range of 10 kHz to 10 Hz. The impedance response at lower frequencies between 10 Hz to 10 mHz is generally attributed to diffusion processes.

Electrode Tensile Property Characterization: The nano-indention test was conducted using a Berkovich nano-indenter (NanoTest Extreme, Micro Materials Ltd, UK). A load was applied to the electrode until it reached 20 mN, then it was held for 300 s to make sure the creep exponent has been removed during unloading. A thermal drift correction was followed for the 60 s after removing the load. For each electrode, 20 indentations were performed to produce statistically reproducible results.

SEM and Focused ion beam-scanning electron microscopy (FIB-SEM) Characterization: After completion of cycling the cell was disassembled in a glove box under an argon atmosphere. SEM characterization was performed with field-emission SEM microscope (Sigma, Carl Zeiss, Germany) equipped with an Energy Dispersive Spectrometer (EDS) (Xmax 50, Oxford Instruments). Cycled electrodes were then transferred to the FIB-SEM (Scios, FEI) instrument for cross-sectional analysis

and tomography, to understand the microstructural evolution of the Si-MOF electrodes. Two-dimensional (2D) analysis is insufficient to fully characterize the complex evolution in the pore shape characteristics of the electrodes.[23],[37]–[39] To overcome the limitations of 2D analysis, three-dimensional (3D) characterization using FIB-SEM tomography was employed. 3D data sets were collected automatically using 'slice and view' software (FEI) where images were recorded using multiple detectors after each slice milled by the FIB. An ion beam voltage of 30 kV and an electron beam voltage of 1 kV was used throughout. Prior to running 3D acquisitions in an electrode, a platinum layer with a nominal thickness of 1 μm was deposited on the sample surface using the ion beam. A U-shaped cut was made around the platinum layer to isolate the volume to be analyzed. Initially a 30 nA ion beam current was used as a rough cut but this was sequentially reduced to 7 nA, 3nA and then 1 nA to polish the sides on the isolated volume. The cut was reasonably large in order to enhance the quality of the SEM images and also to maximize the field of view. For generating the 3D volume of data, an ion beam current of 1 nA was used to cut the 200, 50 nm thick slices contained in a typical data stack. SEM image were captured after every slice with 25 μs dwell time and using multiple detectors. The detectors used for this study was the Everhart-Thornley Detector (ETD) and the Ion Conversion and Electron (ICE) detector for secondary electrons. The reconstructed 3D volume has a lateral (x-y spatial resolution) resolution between 16 nm to 35 nm along with the longitudinal (z spatial resolution) resolution of 50 nm. The spatial distributions of pore phase and solid phase (including the active material, carbonaceous additives, and binder) were then reconstructed. Two fiducial markers were placed inside the field of view to reset any drift that occurs during data collection. Fiducial-1 marker, on the surface of the electrode, was for aligning the ion beam during milling whilst the Fiducial-2 marker in the cross-section was for electron beam alignment. This reduces the amount of misalignment between images and in this case negated the requirement for a data alignment process. The stack of SEM images were converted into a 3D volume and used to reconstruct both the pore volume and bulk material.

Image Processing: The SEM images from FIB-SEM were initially processed by merging the ETD images and ICE images. Then they were further processed by histogram equalization and then by

median noise filtering. This resulted in a smooth image with sharp edges that were subsequently converted to a binary image (white and brown) by applying threshold segmentation in Avizo (FEI). The brown represents pores and white the solid phase, *i.e.* silicon, carbonaceous materials, binder, and MOF. There is no manual segmentation involved, a process which in addition to being labour intensive could add a bias to the data analysis. From the reconstructed 3D volume, analysis on phase volume and surface area were made using Avizo (FEI) whereas tortuosity was calculated by open source *TauFactor*. *TauFactor* was employed within MATLAB for simulation of τ, where the binary segmented 3D reconstructed volume was the input.[25]

RESULTS AND DISCUSSIONS

Electrochemical Cycling Performance

To understand the benefits of MOFs a systematic study was carried out by comparing MOF-modified anodes with control formulations (ZrO_2 and without any additive). ZrO_2 was chosen as an electrochemically inert ceramic additive, containing the same chemical elements as the two MOFs (UiO-66 and UiO-67), whilst a synthetic flake graphite was used in the formulation with no additive. The formulation ratio of electrode slurry used was Si: binder: carbon-mixture: additive: 70:7:11:12 (wt. %). Figure 1b shows the distribution of silicon, MOFs and carbonaceous particles in the electrode slurry prepared after drying as seen by scanning electron microscopy (SEM).

Galvanostatic cycling results are plotted in Figure 1d-f. Cells were cycled at the full capacity of silicon and also at lower capacity limits to compare the effects of these additives towards capacity retention and cycle life. From Figure 1d,e it can be observed that the capacity of the cell decreases over longer cycling, as expected for such devices. The cells cycling at the full experimental capacity of silicon show obvious capacity fade effects after 70 cycles (Figure 1d) whilst for the cells cycling at the half experimental capacity of silicon it is prolonged to more than 90 cycles (Figure 1e). The main reason for this effect can be attributed to breaking down and continual growth of SEI, which in turn results in pore clogging and an increased resistance for Li^+ ion movement.[18],[19] From the cycling profiles, it is evident that incorporation of the MOFs in the Si anode has a significant positive effect on stabilizing the

electrode. Furthermore, the capacity fade is delayed as the capacity limit is reduced from 3579 $mAhg^{-1}$ to 1800 $mAhg^{-1}$ and then further to 1200 $mAhg^{-1}$. The fact that UiO-67 shows superior additive properties in comparison to UiO-66 could be attributed to an increased innate structural flexibility (owing to the nature of the more extended organic linker: see below for a description of the structure) and larger pore size (see Figure 2a,b). This could allow freer movement of Li^+ ions throughout the bulk of the electrode material by a small reduction in tortuosity. In this sense these pores also help to maintain sufficient void structure around the active particles, providing "ion-conducting channels" to the electrode architecture. This is evident from the cell with UiO-67 cycling at the half capacity limit of silicon.

In Figure 1e, it can be shown how the anode with UiO-66 also outperformed the non-modified anode before starting to degrade after 40 cycles. This could be related to the smaller pore sizes (compared to UiO-67) and relatively rigid framework resulting in higher tortuosity for Li-ion transport and thus increasing cell resistance. From Figure 1f it is seen that all the formulations cycled reversibly up to 100 cycles with 1200 $mAhg^{-1}$ capacity limit. However, the UiO-67 additive has better longevity compared to UiO-66. In order to understand lithium interaction with the MOFs used within the same cut-off voltages, MOF-only electrodes were prepared from 80% MOF, 10% binder and 10% carbon black. It can be observed from Figure 1g that UiO-66 can contribute about 271.67 $mAhg^{-1}$ while UiO-67 contributes to 387.34 $mAhg^{-1}$ with a large first cycle loss of 242.92 $mAhg^{-1}$ and 354.58 $mAhg^{-1}$, respectively. The reversible capacity obtained from the MOF-only electrodes was lower than reported in a previous study[11] and this is due to the different operating voltage cut-offs. Tang *et al.*[11] cycled UiO-66 cells between 0.01 V to 3 V *vs* Li/Li^+ whereas in our study the cells were cycled between 0.05 V to 1 V *vs* Li/Li^+. Further electrochemical analysis of MOF-dominant electrodes is presented in Figure S9-S11 in the supplementary section.

Electrode Flexibility Test

UiO-66 consists of $[Zr_6O_4(OH)_4]^{12+}$ metal nodes connected by 1,4-benzenedicarboxylate organic linkers, forming an open-framework containing two distinct cages, tetrahedral and octahedral, with pore diameters of 0.85 nm and 1.15 nm, respectively[20],[21] (see Figure 2a). UiO-67 has an isoreticular structure except that it is connected by the more extended biphenyl-4, 4'-dicarboxylate linkers forming tetrahedral and octahedral pores with diameters 1.15 nm and 2.15 nm, respectively[21] (see Figure 2b). Figure 2c shows a plot of depth *vs* load from nano-indentation tests. Hardness and Young's modulus are calculated using data taken from the slope of the tangent to the unloading curve, summarized as Table 1. Young's modulus is an intrinsic property of the material and it can be observed from Table 1 that the formulation with UiO-67 shows diminished reduced Young's modulus in comparison to other additives. Therefore, we can postulate that the UiO-67 provides an effective inclusion to accommodate volume expansion stresses from silicon upon cycling. In comparison to UiO-66,[30] there is enhanced performance from maintaining the structural integrity of the electrode with UiO-67, as observed in cycling data in Figure 1d-f.

Table 1: Maximum contact depth, hardness and Young's modulus achieved from nano-indentation tests.

Additive	**Maximum Depth [µm]**	**Hardness [GPa]**	**Reduced Young's Modulus [GPa]**
UiO-66	4.62 ± 0.20	0.041 ± 0.003	4.00 ± 0.25
UiO-67	5.04 ± 0.50	0.035 ± 0.007	3.92 ± 0.80
ZrO_2	4.08 ± 0.20	0.053 ± 0.005	5.09 ± 0.39
No additive	5.11 ± 0.19	0.033 ± 0.002	3.55 ± 0.38

Microstructural Evolution using FIB-SEM

FIB-SEM tomography allows three-dimensional (3D) visualization and quantification of geometrical parameters such as thickness, pore surface area, phase volume fraction and tortuosity for a better understanding of the cell performance and its microstructural evolution.[23] Tomography was performed on the pristine and aged electrodes (after 100 cycles). The region of interest for our samples ranged between 25 × 20 μm^2 to 25 × 46 μm^2; since the cycled electrodes had a variable change in thickness of the electrode. From there we obtained a 3D reconstructed volume of 20 × 15 × 10 μm^3 for all the samples (Figure 3).

The porosity retention is higher in the MOF electrodes in comparison to the control electrodes. It can be seen that the porosity of the cycled electrodes at half capacity has decreased by only 31% and 22% for the UiO-66 and UiO-67, respectively (see Figure 4a) with respect to their pristine electrode. Reduced porosity or increased tortuosity may adversely affect the lithium permeability and diffusion into the active material, resulting in capacity decay or loss. The observation of cracks on the electrode surface is consistent with previously reported studies.[31–33] This observation can also be supported by the impedance study (see Figure 5) and tortuosity factor (see Figure 4i) for the electrodes.

The initial thickness of the pristine electrode was recorded as well as the post-cycling thickness. There is an incremental change in the thickness of electrode cycled at half capacity by >50% in the control samples compared with 48% and 38% for the UiO-66 and UiO-67, respectively (see Figure 4b). Another observation that can be made is that electrodes cycled at half capacity have a lower increment in the electrode thickness with respect to electrodes cycled at full capacity of silicon. Comparing the pore surface areas in contact with the electrolyte for a pristine electrode and a cycled electrode, it can be seen that there is a large decrease in specific surface area, around 50% in the control samples compared to *ca* 29% for MOF electrodes at full capacity (see Figure 4c). This means that the surface of the particles has undergone redox reaction, *i.e.* there is continuum formation and growth of SEI.[34] The UiO-67, however, has undergone the least change in pore surface area at half capacity demonstrating a significant advantage of having this MOF in the electrode.

From Figure 4d,e it can be observed that there is a segregation of pore-volume distribution upon cyclic aging. Coalescence among the particles in the cycled electrodes can also be seen, which is likely from the huge volume expansion and electrochemical fusion of silicon particles - similar to observations made in the previous studies.[33] It has been reported elsewhere that silicon has a tendency to fuse together upon electrochemical cycling.[35] The observed changes in porosity are likely to impact the permeability towards the electrolyte solvents and be responsible for the eventual decay in performance of the anode.

There is a significant change in the pore size and distribution after 100 cycles for each of the electrode formulations. Upon aging, there is a shift towards the lower end of the pore volume which may be an indication that the macropores are becoming filled with detached SEI products upon cycling (see Figure 4f,g). However, on careful observation in Figure 4d,e it can be seen that there are many pores with large volume (*i.e.* towards the right-hand side of the distribution) which can be explained by the large volume expansion that active silicon particles undergo. This correlates with the decrease in charge transfer impedance upon full capacity cycling (see later in Figure 5j). From Figure 4e it can be seen that electrodes with UiO-66 and no additive have a higher volume percent of lower pores compared to UiO-67 electrode attributing to the Si-fusion and subsequent pulverization from large volume expansion resulting in microstructure fragility. Therefore, it can be concluded that the UiO-67 acts as a flexible pore channel for the active silicon particle undergoing volume changes upon lithiation/de-lithiation and maintaining "ion-conducting channels" for the electrolytes. From Figure 4 there is a direct evidence of UiO-67 as the superior additive. This may be ascribed to it having larger pore diameter, and a longer organic linker than UiO-66 to provide a more flexible structure to absorb the continuous strain from silicon particle upon cycling.

Tortuosity Factor (τ) Calculation

τ is an important parameter that provides information on resistance to ionic transport property of ions through pores. τ was calculated by simulating the steady-state diffusion flow through the 3D pore network.[36] From Figure 4i, it can be seen that τ values for each of the electrodes have decreased upon cycling at half capacity, except for the formulation with no additive. The explanation for this is that in the absence of any cushioning additive effect which can help to sustain the volume changes, the

mesopores are filled by fragmented SEI layers. For electrodes with MOF additives, τ decreases, as the volume changes from silicon particles have resulted in macro-voids and we propose that these cracks act as carrier path for the electrolyte. The architectural degradation is minimal in the MOF-containing anodes as inferred from impedance measurement and also reflected in the τ values (see Figure 5). Therefore, the gradual decrease in pore volume from broken SEI would thereby impede the flow of Li^+ ions through the porous network. Formulations with UiO-66 and UiO-67 when cycled at full capacity have lower τ when compared to the cells cycled at half capacity since the former has undergone macro cracking with large volume changes with silicon's expansion. This observation is also supported by impedance measurements (see Figure 5j).

Electrochemical Impedance Investigations

Nyquist plots obtained from PEIS provide information on the kinetics of the reaction and diffusion processes corresponding to certain frequency ranges.[37–39] The two features occurring in the high-frequency range correspond to interfacial phenomena, the first can be attributed to an insulating SEI layer, while the second to charge transfer (CT) resistance.[39] R_{SEI} gradually increases with the cycle number, which indicates that the SEI layer is continuously growing because of the large volume changes. Thus, one hypothesis we can make is that fragments of the SEI layer break from the surface and migrate to the pores in the electrode and continue to accumulate as a function of aging.[19],[26] This phenomenon has a strong influence on the impedance of the electrode and is very evident from Figure 5i,l. During this aging period, where the thick SEI layer breaks off, there is re-formation of a new SEI layer and therefore, an increased series resistance from pore clogging. This formation of new SEI results in consumption of Li^+ ions which should result in capacity loss; however, in the present study, we have an excess of Li^+ ions from the Li foil used in a half cell. Upon cycling, the consumption of Li^+ ions in the SEI layer reduces its concentration in the electrolyte and it is reflected in the slight increase in ionic resistivity, *i.e.* R_{series}. The segregated pores and heterogeneous distribution of the pores from FIB-SEM results (see Figure 4d,e) hinder the passage of intercalating Li^+ ions resulting in an increased resistance. The equivalent circuit used for this calculation is shown in Figure 5g where the capacitance of the SEI

layer and the capacitance of the double layer are denoted by constant phase elements CPE_1 and CPE_2, respectively.

Figure 5h-m shows the resistance values for all the different formulation and it can be observed the Si-MOF electrodes showed less resistance in comparison to the control electrode. For the control electrodes with no additive, cycled at half capacity of silicon the impedance gradually increased until 70 cycles and after which there was huge resistance increase: this is likely to be due to the continuum growth of an insulating (SEI) layer and high charge transfer resistance, which is entirely consistent with the cyclic data (see Figure 1d-f). The R_{CT} for cells cycled at full capacity of silicon tends to decreases after 50 cycles for all of the formulations (Figure 5j) and can be explained as a result of large cracks that have resulted in the electrode's structure due to huge periodic volume changes from silicon particles. The CT process involves two steps, namely, de-solvation of the solvated Li^+ ions in the electrolyte and transportation of these Li^+ ions through the SEI layer until it accepts an electron at the electrode's surface[40]. The large voids allow comparatively easy transportation of electrolyte within the electrode and thereby facilitate the availability of Li^+ ions to diffuse through the active particles. The large cracks also result in a fresh surface for further side reactions, increasing the R_{SEI} which also increases the R_{series} as they reduce the electrical conductivity of the electrode as a whole.

CONCLUSIONS

The porous zirconium carboxylate MOFs UiO-66 and UiO-67 as additives in Si-based anodes have the dual purpose of improving and maintaining the porous nature of composite battery materials. It has proven possible to improve the performance of a silicon electrode by the homogeneous inclusion of MOFs with large pore size acting as "ion-conducting channels" via their flexible structures. The highly reversible electrochemical performance of the silicon electrodes that incorporate MOFs as additives significantly improve cell performance, especially with UiO-67. The MOFs can act as lithium hosts, contributing up to 387 $mAhg^{-1}$ of capacity when cycled *vs* Li/Li^+, but more importantly, the flexible frameworks of MOFs are able to maintain a high degree of porosity upon battery cycling, overcoming pore blockage and increased tortuosity that usually takes place in silicon anodes due to large volume changes on alloying/de-alloying. We propose that these findings provide a novel perspective towards

robust Si anodes for use in LIB materials, which could be tuned further by hierarchical modification of the porosity of MOFs, combined with a judicious choice of the functionalized ligands to provide compatibility with the anode components. Optimising the current formulation ratios will be the next phase of the study for further performance optimisation and we intend to perform these experiments in the future.

AUTHOR INFORMATION

Corresponding Authors

*E-mail (Richard I. Walton): r.i.walton@warwick.ac.uk

Author contributions

M.J.L and R.I.W. conceived the idea of incorporating the metal-organic frameworks (MOFs) into silicon-based anode for lithium-ion batteries. L.J.W. synthesised UiO-66 and UiO-67 MOFs and conducted XRD for the MOFs and all the electrode materials. L.J.W. and R.M. carried out the coin cell making and electrochemical measurements of the electrode materials. R.M. conducted FIB-SEM characterisation and image processing. Q.H. performed the nano-indentation measurements. All authors participated in the analysis of the experimental data, the discussions of the results and the preparation of the paper. R.B., P.R.S. and G.W. provided advice and helped in editing the manuscript. All authors have given approval to the final version of the manuscript.

Notes

The authors declare no competing financial interests.

ACKNOWLEDGEMENTS

The authors would like to thank the University of Warwick Materials Global Research Priority for award of a summer bursary for L.J.W. The authors would also like to acknowledge funding from AMorpheuS project (Grant Reference EP/NO01583/1) and the Faraday Institution Degradation Fast Start project (Grant Reference RG94392). The authors are grateful to David Walker of the University of Warwick X-ray diffraction facility for providing assistance in data collection.

SUPPORTING INFORMATION

Additional details, including: XRD patterns, SEM images with EDS mapping and TGA plots. Additional tomography reconstruction of cycled electrodes.

REFERENCES

(1) Li, J.; Dahn, J. R. An In Situ X-Ray Diffraction Study of the Reaction of Li with Crystalline Si. *J. Electrochem. Soc.* **2007**, *154* (3), A156.

(2) Obrovac, M. N.; Krause, L. J. Reversible Cycling of Crystalline Silicon Powder. *J. Electrochem. Soc.* **2007**, *154* (2), A103.

(3) Maranchi, J. P.; Hepp, A. F.; Kumta, P. N. High Capacity, Reversible Silicon Thin-Film Anodes for Lithium-Ion Batteries. *Electrochem. Solid-State Lett.* **2003**, *6* (9), A198.

(4) Ohara, S.; Suzuki, J.; Sekine, K.; Takamura, T. A Thin Film Silicon Anode for Li-Ion Batteries Having a Very Large Specific Capacity and Long Cycle Life. *J. Power Sources* **2004**, *136* (2 SPEC. ISS.), 303–306.

(5) Chan, C. K.; Ruffo, R.; Hong, S. S.; Cui, Y. Surface Chemistry and Morphology of the Solid Electrolyte Interphase on Silicon Nanowire Lithium-Ion Battery Anodes. *J. Power Sources*

2009, *189* (2), 1132–1140.

(6) Liu, N.; Lu, Z.; Zhao, J.; McDowell, M. T.; Lee, H.-W.; Zhao, W.; Cui, Y. A Pomegranate-Inspired Nanoscale Design for Large-Volume-Change Lithium Battery Anodes. *Nat. Nanotechnol.* **2014**, *9* (3), 187–192.

(7) Kasavajjula, U.; Wang, C.; Appleby, A. J. Nano- and Bulk-Silicon-Based Insertion Anodes for Lithium-Ion Secondary Cells. *J. Power Sources* **2007**, *163* (2), 1003–1039.

(8) Farooq, U.; Choi, J.-H.; Atif Pervez, S.; Yaqub, A.; Kim, D.-H.; Lee, Y.-J.; Saleem, M.; Doh, C.-H. Effect of Binder and Composition Ratio on Electrochemical Performance of Silicon/Graphite Composite Battery Electrode. *Mater. Lett.* **2014**, *136*, 254–257.

(9) Lestriez, B.; Bahri, S.; Sandu, I.; Roué, L.; Guyomard, D. On the Binding Mechanism of CMC in Si Negative Electrodes for Li-Ion Batteries. *Electrochem. commun.* **2007**, *9* (12), 2801–2806.

(10) Yoshio, M.; Wang, H.; Fukuda, K.; Umeno, T.; Dimov, N.; Ogumi, Z. Carbon-Coated Si as a Lithium-Ion Battery Anode Material. *J. Electrochem. Soc.* **2002**, *149* (12), A1598.

(11) Tang, B.; Huang, S.; Fang, Y.; Hu, J.; Malonzo, C.; Truhlar, D. G.; Stein, A. Mechanism of Electrochemical Lithiation of a Metal-Organic Framework without Redox-Active Nodes. *J. Chem. Phys.* **2016**, *144* (19), 194702.

(12) Zhang, L.; Wu, H. Bin; Lou, X. W. Metal−Organic-Frameworks-Derived General Formation of Hollow Structures with High Complexity. *J. Am. Chem. Soc.* **2013**, *135* (29), 10664–10672.

(13) Xia, W.; Mahmood, A.; Zou, R.; Xu, Q. Metal–organic Frameworks and Their Derived Nanostructures for Electrochemical Energy Storage and Conversion. *Energy Environ. Sci.* **2015**, *8* (7), 1837–1866.

(14) Wang, L.; Han, Y.; Feng, X.; Zhou, J.; Qi, P.; Wang, B. Metal-Organic Frameworks for Energy Storage: Batteries and Supercapacitors. *Coord. Chem. Rev.* **2016**, *307*, 361–381.

(15) Han, Y.; Qi, P.; Zhou, J.; Feng, X.; Li, S.; Fu, X.; Zhao, J.; Yu, D.; Wang, B. Metal-Organic

Frameworks (MOFs) as Sandwich Coating Cushion for Silicon Anode in Lithium Ion Batteries. *ACS Appl. Mater. Interfaces* **2015**, *7* (48), 26608–26613.

(16) Song, J.; Zhou, M.; Yi, R.; Xu, T.; Gordin, M. L.; Tang, D.; Yu, Z.; Regula, M.; Wang, D. Interpenetrated Gel Polymer Binder for High-Performance Silicon Anodes in Lithium-Ion Batteries. *Adv. Funct. Mater.* **2014**, *24* (37), 5904–5910.

(17) García, R. E.; Chiang, Y.-M. Spatially Resolved Modeling of Microstructurally Complex Battery Architectures. *J. Electrochem. Soc.* **2007**, *154* (9), A856.

(18) Huang, Q.; Loveridge, M. J.; Genieser, R.; Lain, M. J.; Bhagat, R. Electrochemical Evaluation and Phase-Related Impedance Studies on Silicon–Few Layer Graphene (FLG) Composite Electrode Systems. *Sci. Rep.* **2018**, *8* (1), 1386.

(19) Komaba, S.; Okushi, K.; Ozeki, T.; Yui, H.; Katayama, Y.; Miura, T.; Saito, T.; Groult, H. Polyacrylate Modifier for Graphite Anode of Lithium-Ion Batteries. *Electrochem. Solid-State Lett.* **2009**, *12* (5), A107.

(20) Obrovac, M. N.; Christensen, L. Structural Changes in Silicon Anodes during Lithium Insertion/Extraction. *Electrochem. Solid-State Lett.* **2004**, *7* (5), A93–A96.

(21) Wilson, J. R.; Kobsiriphat, W.; Mendoza, R.; Chen, H.-Y.; Hiller, J. M.; Miller, D. J.; Thornton, K.; Voorhees, P. W.; Adler, S. B.; Barnett, S. A. Three-Dimensional Reconstruction of a Solid-Oxide Fuel-Cell Anode. *Nat. Mater.* **2006**, *5* (7), 541–544.

(22) Wilson, J. R.; Cronin, J. S.; Barnett, S. A.; Harris, S. J. Measurement of Three-Dimensional Microstructure in a LiCoO2 Positive Electrode. *J. Power Sources* **2011**, *196* (7), 3443–3447.

(23) Ender, M.; Joos, J.; Carraro, T.; Ivers-Tiffée, E. Three-Dimensional Reconstruction of a Composite Cathode for Lithium-Ion Cells. *Electrochem. commun.* **2011**, *13* (2), 166–168.

(24) Etiemble, A.; Tranchot, A.; Douillard, T.; Idrissi, H.; Maire, E.; Roue, L. Evolution of the 3D Microstructure of a Si-Based Electrode for Li-Ion Batteries Investigated by FIB / SEM Tomography. *J. Electrochem. Soc.* **2016**, *163* (8), 1550–1559.

(25) Cooper, S. J.; Bertei, A.; Shearing, P. R.; Kilner, J. A.; Brandon, N. P. TauFactor: An Open-Source Application for Calculating Tortuosity Factors from Tomographic Data. *SoftwareX* **2016**, *5*, 203–210.

(26) Shi, F.; Song, Z.; Ross, P. N.; Somorjai, G. A.; Ritchie, R. O.; Komvopoulos, K. Failure Mechanisms of Single-Crystal Silicon Electrodes in Lithium-Ion Batteries. *Nat. Commun.* **2016**, *7* (May), 1–8

(27) Vetter, J.; Novak, P.; Wagner, M. R.; Veit, C.; Moller, K. C.; Besenhard, J. O.; Winter, M.; Wohlfahrt-Mehrens, M.; Vogler, C.; Hammouche, A. Ageing Mechanisms in Lithium-Ion Batteries. *J. Power Sources* **2005**, *147* (1–2), 269–281.

(28) Katz, M. J.; Brown, Z. J.; Colón, Y. J.; Siu, P. W.; Scheidt, K. A.; Snurr, R. Q.; Hupp, J. T.; Farha, O. K. A Facile Synthesis of UiO-66, UiO-67 and Their Derivatives. *Chem. Commun.* **2013**, *49* (82), 9449.

(29) Cavka, J. H.; Olsbye, U.; Guillou, N.; Bordiga, S.; Lillerud, K. P. A New Zirconium Inorganic Building Brick Forming Metal Organic Frameworks with Exceptional Stability. *J. Am. Chem. Soc.* **2008**, *6*, 1–19.

(30) Wu, H.; Yildirim, T.; Zhou, W. Exceptional Mechanical Stability of Highly Porous Zirconium Metal-Organic Framework UiO-66 and Its Important Implications. *J. Phys. Chem. Lett.* **2013**, *4* (6), 925–930.

(31) Philippe, B.; Dedryveère, R.; Gorgoi, M.; Rensmo, H.; Gonbeau, D.; Edström, K. Role of the LiPF6 Salt for the Long-Term Stability of Silicon Electrodes in Li-Ion Batteries - A Photoelectron Spectroscopy Study. *Chemistry of Materials*. 2013, pp 394–404.

(32) Radvanyi, E.; De Vito, E.; Porcher, W.; Jouanneau Si Larbi, S. An XPS/AES Comparative Study of the Surface Behaviour of Nano-Silicon Anodes for Li-Ion Batteries. *J. Anal. At. Spectrom.* **2014**, *29* (6), 1120–1131.

(33) Radvanyi, E.; Porcher, W.; De Vito, E.; Montani, A.; Franger, S.; Jouanneau Si Larbi, S. Failure

Mechanisms of Nano-Silicon Anodes upon Cycling: An Electrode Porosity Evolution Model. *Phys. Chem. Chem. Phys.* **2014**, *16* (32), 17142–17153.

(34) Bordes, A.; Eom, K.; Fuller, T. F. The Effect of Fluoroethylene Carbonate Additive Content on the Formation of the Solid-Electrolyte Interphase and Capacity Fade of Li-Ion Full-Cell Employing Nano Si-Graphene Composite Anodes. *J. Power Sources* **2014**, *257*, 163–169.

(35) Karki, K.; Epstein, E.; Cho, J. H.; Jia, Z.; Li, T.; Picraux, S. T.; Wang, C.; Cumings, J. Lithium-Assisted Electrochemical Welding in Silicon Nanowire Battery Electrodes. *Nano Lett.* **2012**, *12* (3), 1392–1397.

(36) Cooper, S. J.; Eastwood, D. S.; Gelb, J.; Damblanc, G.; Brett, D. J. L.; Bradley, R. S.; Withers, P. J.; Lee, P. D.; Marquis, A. J.; Brandon, N. P.; et al. Image Based Modelling of Microstructural Heterogeneity in LiFePO4 Electrodes for Li-Ion Batteries. *J. Power Sources* **2014**, *247*, 1033–1039.

(37) Zhang, S. S.; Xu, K.; Jow, T. R. Electrochemical Impedance Study on the Low Temperature of Li-Ion Batteries. *Electrochim. Acta* **2004**, *49* (7), 1057–1061.

(38) Chen, L.; Wang, K.; Xie, X.; Xie, J. Effect of Vinylene Carbonate (VC) as Electrolyte Additive on Electrochemical Performance of Si Film Anode for Lithium Ion Batteries. *J. Power Sources* **2007**, *174* (2), 538–543.

(39) Eom, K.; Joshi, T.; Bordes, A.; Do, I.; Fuller, T. F. The Design of a Li-Ion Full Cell Battery Using a Nano Silicon and Nano Multi-Layer Graphene Composite Anode. *J. Power Sources* **2014**, *249*, 118–124.

(40) Jow, T. R.; Delp, S. A.; Allen, J. L.; Jones, J.-P.; Smart, M. C. Factors Limiting Li+ Charge Transfer Kinetics in Li-Ion Batteries. *J. Electrochem. Soc.* **2018**, *165* (2), A361–A367.

Figure Captions

Figure 1. SEM images and specific discharge capacity (based on active mass of silicon) profiles at the different capacity limits. SEM image of (a) only UiO-67 MOF; (b,c) UiO-67 in Si electrode with energy dispersive spectra (EDS) derived chemical distribution maps showing the presence of Zr-based MOF (UiO-67) in the electrode slurry as shown in (c); specific discharge capacity at (d) full capacity of silicon (3579 $mAhg^{-1}$) (e) half capacity of silicon (1800 $mAhg^{-1}$) (f) one-third capacity of silicon (1200 $mAhg^{-1}$) (longer cycling of Si-MOFs are shown as the inset) (g) first lithiation-delithiation voltage profiles for MOFs. The legends for (d) also applies to (e-g).

Figure 2. Crystal structures of the MOFs (a) UiO-66 and (b) UiO-67. c) Tensile curves from nano-indentation test. In (a) and (b) the blue polyhedral represent Zr-centred oxy coordination polyhedra, and the yellow spheres represent the maximum free pore space.

Figure 3. 3D FIB-SEM tomography reconstruction of Si-MOF electrodes. a) SEM image of the electrode after the final polishing step with two fiducial markers, (b) schematic representation of FIB-SEM imaging process; the greyscale 3D reconstructed volume of the electrode with (c) UiO-67, (d) no additive, before and after cycling at full capacity for 100 cycles.

Figure 4. Geometrical property comparison at silicon's half and full capacity cycling. Electrode's (a) porosity, (b) thickness and (c) pore surface area comparison. Cumulative pore size distribution comparison of all cycled electrodes with (d) half capacity of silicon, (e) full capacity of silicon and individually for (f) no additive, (g) UiO-66, (h) UiO-67 electrodes. i) Tortuosity factor comparison between pristine electrodes and cycled electrodes after 100 cycles at Si's half and full capacity cycling, (j) color map of diffusion simulation with red as high flux density regions for full capacity cycling of UiO-67 and no additive electrodes. The legends for (a) also applies to (c,d).

Figure 5. Nyquist plots and impedance fitting results. Nyquist plots during the charging process for all formulations cycled with full capacity of silicon (3579 $mAhg^{-1}$) after (a) 10 cycles, (b) 50 cycles and (c) 100 cycles; with half capacity of silicon (1800 $mAhg^{-1}$) after (d) 10 cycles, (e) 50 cycles and (f) 100 cycles (zoom-in plot shown as the inset). g) The electrochemical equivalent circuit used for fitting the Nyquist plots; and the impedance fitting result comparison between (h-j) 3579 $mAhg^{-1}$ and (k-m) 1800 $mAhg^{-1}$ against (h,k) Series resistance (i,l) SEI resistance (j,m) interphase contact and charge transfer resistance (a reconstruction of the degradation methods during cycling are illustrated with schematics as the insets and a more comprehensive description of these is presented in Figure S13). The legends for (a) also applies to (b-c, h-j) whilst the legend for (d) further applies to (e-f, k-m).

Table of Contents Graphic

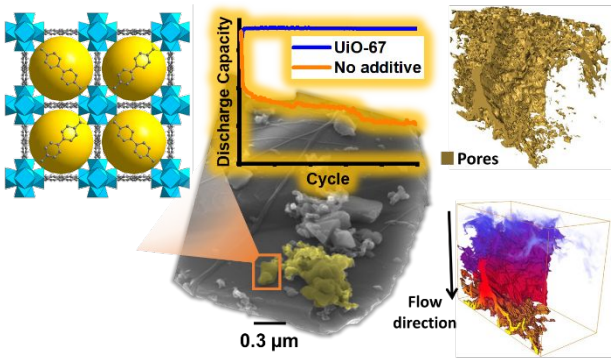

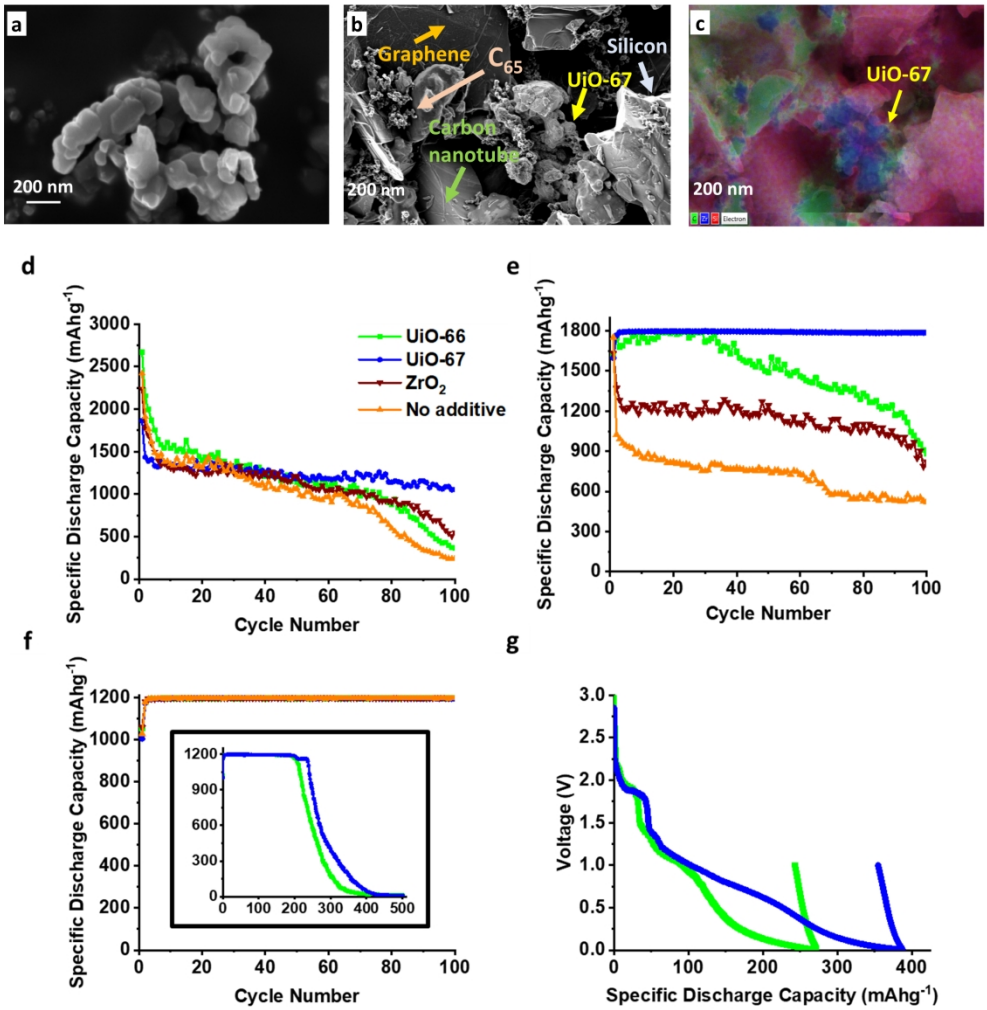

432x435mm (150 x 150 DPI)

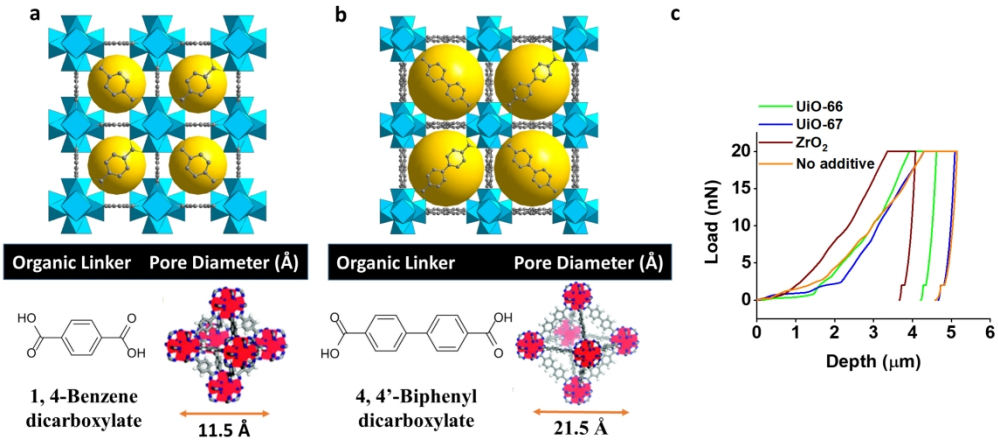

420x194mm (150 x 150 DPI)

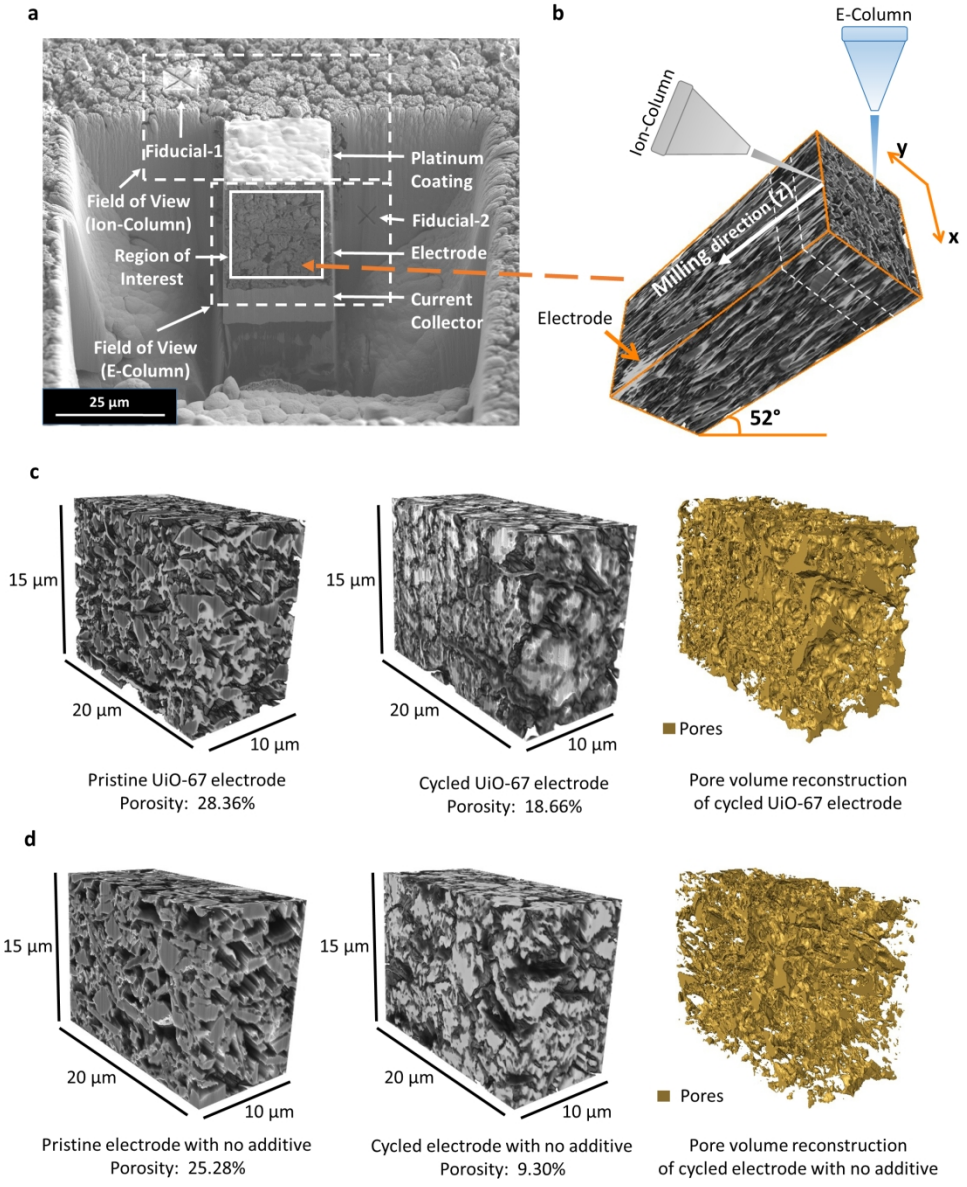

359x438mm (150 x 150 DPI)

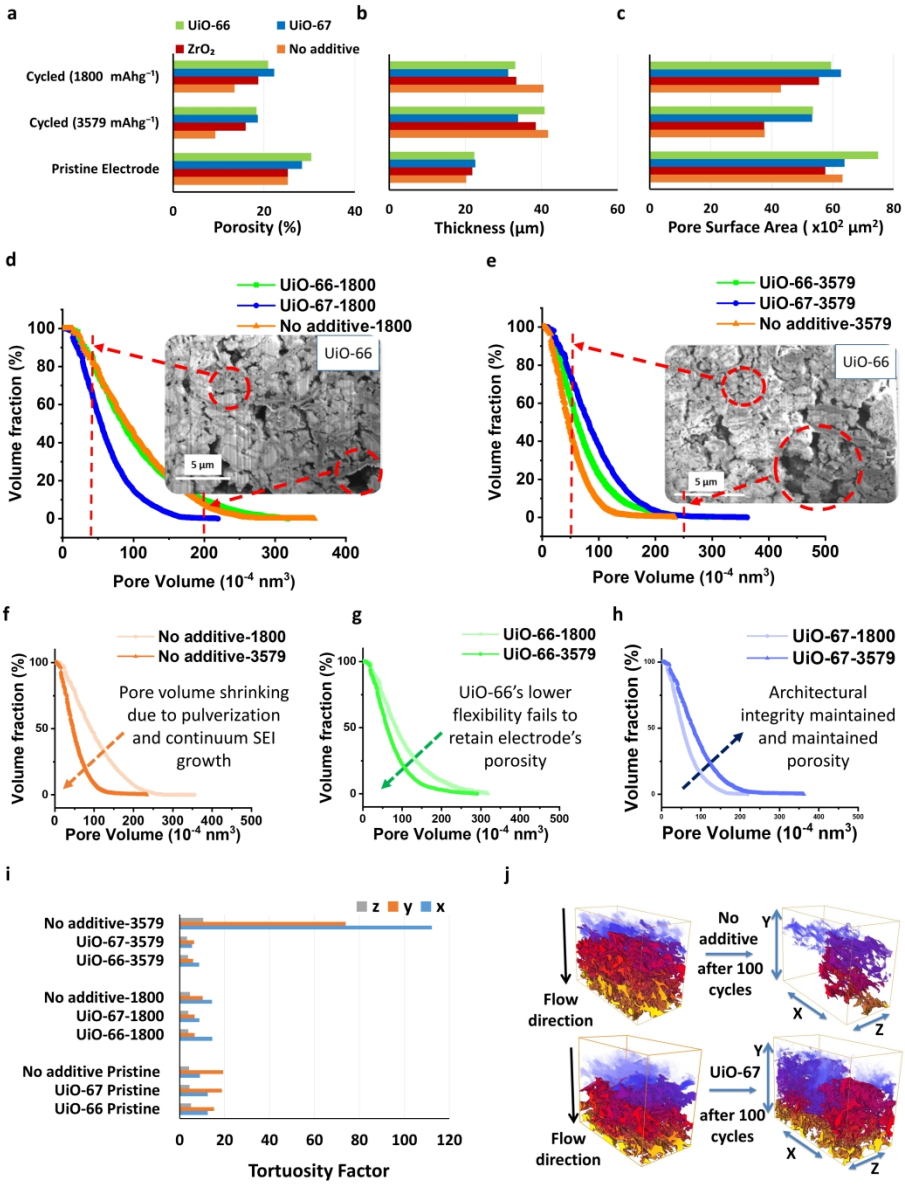

618x803mm (150 x 150 DPI)

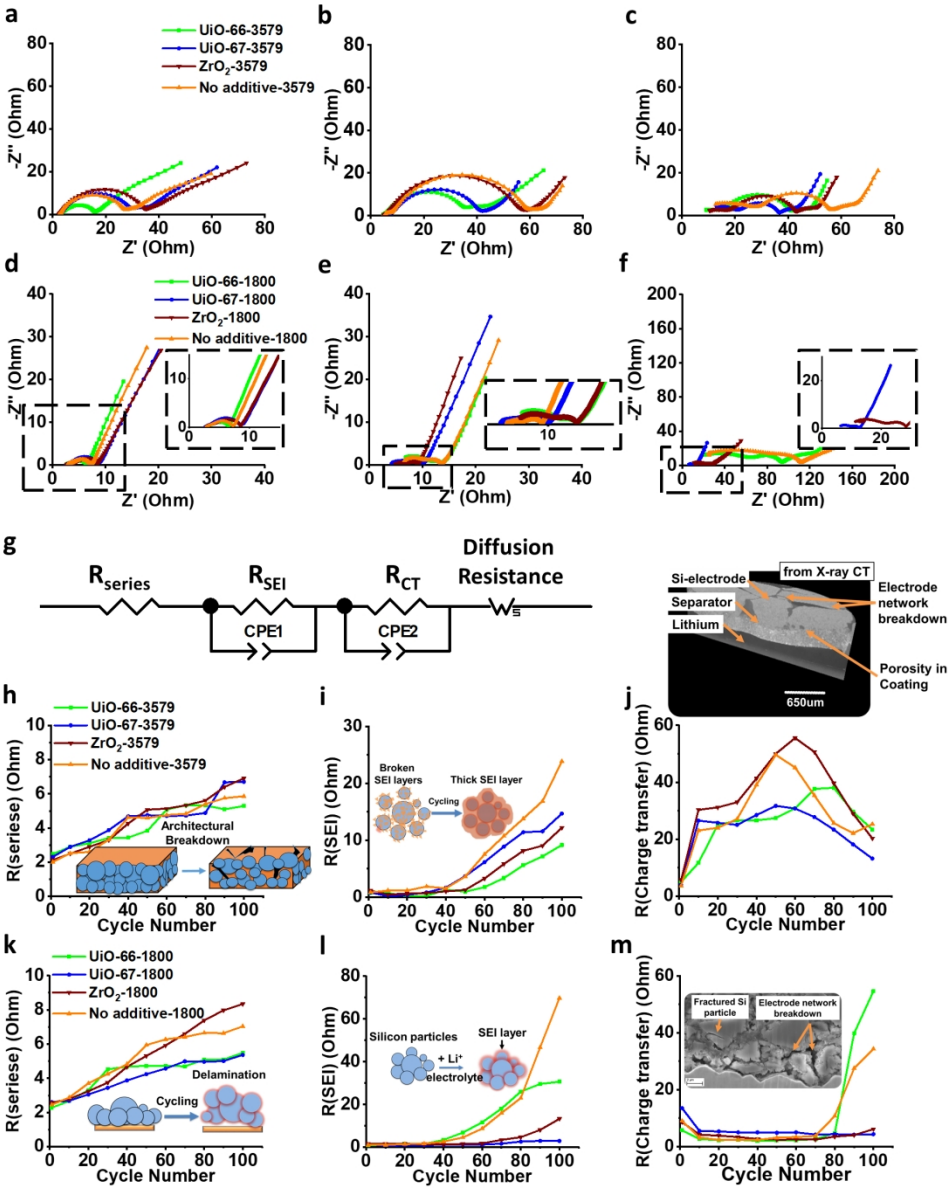

336x418mm (150 x 150 DPI)